Chemical Science

ROYAL SOCIETY OF CHEMISTRY

EDGE ARTICLE

View Article Online
View Journal | View Issue

Cite this: *Chem. Sci.*, 2026, **17**, 6536

All publication charges for this article have been paid for by the Royal Society of Chemistry

A dual-function molecule enables stable four-electron conversion and Zn deposition for high-capacity aqueous Zn–I_2 batteries

Huiquan Zhang,[a] Xueying Zhang,[a] Dongmin Ma,[a] Xinxin Cai,[a] Mochi Lv,[a] Hongting Yan,[a] Junbo Niu[b] and Weixing Song *[a]

Received 8th January 2026
Accepted 1st February 2026

DOI: 10.1039/d6sc00182c

rsc.li/chemical-science

Aqueous zinc–iodine batteries (ZIBs) are a promising energy storage technology due to the abundance of iodine, environmental friendliness, and low cost. This study introduces a multifunctional additive, L-lysine hydrochloride (LLH), designed to activate the four-electron transfer chemistry between I^+ and I^- species, significantly boosting energy density. LLH stabilizes I^+ *via* dual coordination from the amino groups and chloride ion, effectively suppressing hydrolysis and enabling reversible $2I^-/I_2^0/2I^+$ conversion. The preferential adsorption of the carboxyl group of protonated L-lysine at the zinc anode promotes uniform zinc deposition while inhibiting the hydrogen evolution reaction. Additionally, the incorporation of LLH effectively suppresses the shuttle effect by interacting with iodine species through its carboxyl and amino groups. LLH-modified Zn||Zn symmetric batteries demonstrate extended cycling stability, operating beyond 4000 hours, while Zn||I_2 full batteries deliver a high specific capacity of 502 mAh g^{-1} at 1 A g^{-1}. This additive strategy renders a facile and efficient approach to realizing high-capacity and durable ZIBs.

Introduction

Aqueous zinc–iodine batteries (ZIBs) have garnered significant attention due to their higher theoretical specific capacities and abundant resource potential compared to conventional intercalation-type electrodes.[1–8] The redox reaction based on the $2I^-/I_2^0$ couple is commonly employed at the cathode, offering a theoretical capacity of 211 mAh g^{-1}. However, its energy density and output voltage in conventional two-electron aqueous zinc–iodine batteries (2eZIBs) remain suboptimal. The $2I^-/I_2^0$ conversion generates water-soluble polyiodide intermediates, inducing a shuttle effect that causes irreversible active material loss and reduces I_2 utilization.[9–12] ZIBs also face limitations from conventional aqueous electrolytes, including the hydrogen evolution reaction (HER), corrosion, passivation at the Zn anode/electrolyte interface, and dendritic Zn growth due to inhomogeneous electric field distribution.[13–18] Recently, four-electron aqueous zinc–iodine batteries (4eZIBs) based on sequential $2I^-/I_2^0/2I^+$ redox pairs have attracted extensive research interest, delivering enhanced specific capacities (422 mAh g^{-1}) and higher operating voltage platforms to achieve superior energy density.[19–21] Nevertheless, thermodynamic instability of I^+ and unstable Zn plating/stripping in conventional electrolytes pose significant challenges. Issues such as active iodine dissolution and polyiodide shuttling further hinder the practical implementation of 4eZIBs.[22]

Recent studies have reported some strategies to activate high-valent iodine redox reactions for high-theoretical-capacity aqueous Zn||I_2 batteries. These studies typically utilize relatively high concentrations of halide ions to form halides on the cathode side (such as introducing Cl^- to combine and form ICl).[22,23] A high-concentration electrolyte containing 19 M LiCl, 19 M $ZnCl_2$, and 8 M acetonitrile was developed to suppress I^+ hydrolysis while supplying abundant free Cl^- for facilitating $2I^-/I_2^0$ conversion.[24] However, high Cl^- concentrations corrode battery components, while insufficient Cl^- fails to fully stabilize I^+, leading to hydrolysis and limited capacity. A ternary hydrated eutectic electrolyte comprising dimethyl sulfone, nicotinamide, and $Zn(ClO_4)_2 \cdot 6H_2O$ was used to stabilize electrophilic I^+, which extends the electrochemical window.[25] But high-concentration salts or eutectic electrolytes undermine the cost-effectiveness of aqueous systems and reduce their inherent ionic conductivity.

As an electrolyte additive distinct from conventional amino acid-based ones, L-lysine hydrochloride (LLH) is herein utilized to both stabilize the zinc anode and boost cycling performance, as well as anchor I^+ species to realize reversible $2I^-/I_2^0/2I^+$ redox conversion. Compared to an electrolyte modified with HCl at an equivalent additive concentration, LLH exhibits stronger anchoring capability towards I^+ species, which can effectively prevent its hydrolysis and enhance the cycling performance of

[a]*Department of Chemistry, Capital Normal University, Beijing 100048, P. R. China. E-mail: songwx@cnu.edu.cn*

[b]*School of Materials Science and Engineering, Nanyang Technological University, 50 Nanyang Avenue, Singapore 639798, Singapore*

Zn||I_2 batteries. Experimental analyses and density functional theory (DFT) calculations reveal that LLH anchors I^+ *via* the synergistic effect of the nucleophilic amino groups and chloride ion, suppressing hydrolysis, thermodynamically favoring iodine valence transitions, enhancing redox kinetics and reversibility, and mitigating the shuttle effect. Preferential adsorption of protonated L-lysine (LL^+) on the Zn anode modulates the inner Helmholtz plane (IHP), extends the stable electrochemical window, and achieves highly reversible Zn plating/stripping with stable cycling over 4000 h. A typical Zn||I_2 battery with the LLH additive demonstrates an increased specific capacity of 502 mAh g^{-1} at 1 A g^{-1} and an average coulombic efficiency (CE) of 99.4% at 5 A g^{-1}.

Results and discussion

Electrochemical performance of the LLH-optimized electrolyte for the $2I^-/I_2^0/2I^+$ reaction

LLH is employed as an additive in 2 M $ZnSO_4$ electrolyte (Fig. 1a) where the amino groups and chloride ion of LLH coordinate with I^+ species to stabilize iodine intermediates at the cathode interface, thereby enabling stable four-electron transfer and an attendant enhancement in energy density. Simultaneously, LLH can coordinate with various iodine species, thereby suppressing polyiodide formation. Furthermore, preferential adsorption at the anode interface reduces reactive water population in the IHP, effectively suppressing the HER and passivation processes. The interfacial regulation further promotes homogeneous zinc deposition and inhibits dendritic growth. The optimal LLH concentration of 500 mM in $ZnSO_4$ electrolyte ($ZnSO_4$/LLH) is determined through anode electrochemical screening (Fig. S1). The performance degradation with shortened lifespan of the battery with more than 500 mM LLH in the $ZnSO_4$ electrolyte is likely caused by increased Cl^- concentration; therefore, 500 mM LLH was selected for further research.

Distinct charge/discharge plateaus corresponding to $I_2^0/2I^+$ conversion are observed in $ZnSO_4$/LLH electrolytes (Fig. 1b). Notably, a discharge capacity of 495 mAh g^{-1} is achieved at 2 A g^{-1}. The specific capacity of the Zn||I_2 batteries exceeds the theoretical value of 422 mAh g^{-1} due to capacitive contributions from the activated carbon substrate in the cathode (Fig. S2). The observed capacity significantly exceeds that of the $ZnSO_4$ electrolyte, which can be attributed to the four-electron redox conversion ($2I^-/I_2^0/2I^+$). This result demonstrates the effectiveness of LLH-mediated suppression of I^+ hydrolysis. Compared to the HCl-modified electrolyte at an equivalent concentration, LLH delivers higher capacity, demonstrating the superior I^+ anchoring capability of LLH relative to HCl. Cyclic voltammetry (CV) curves exhibit two redox peak pairs (1.77/1.62 V and 1.27/1.14 V) for four-electron transfer reactions. These features align with galvanostatic charge/discharge (GCD) curve profiles and are assigned to $I_2^0/2I^+$ and $2I^-/I_2^0$ conversions (Fig. S3).[26] The $I_2^0/2I^+$ reduction peak in $ZnSO_4$/LLH shows higher current density and a larger area than those in $ZnSO_4$/HCl. Moreover, smaller redox potential gaps in $ZnSO_4$/LLH indicate improved reversibility compared to other electrolytes. Lower Tafel slopes for $I_2^0/2I^+$ and $2I^-/I_2^0$ conversions in $ZnSO_4$/LLH confirm accelerated reaction kinetics (Fig. S4).[9] A significant reduction in the Tafel slope of the R2 peak suggests highly reducibility and reversibility of the anchored I^+ species.

To further investigate the electrochemical reaction kinetics in the $ZnSO_4$/LLH electrolyte, we conducted CV measurements at various scan rates (Fig. 2a). The contributions of surface-controlled capacitances can be qualitatively analyzed based on the relationship between the measured current (i) and scan rate (v) from the CV curves: $i = av^b$. When b is close to 1.0, the electrochemical behavior is dominated by a surface capacitive process, whereas when b approaches 0.5, a diffusion-controlled process is observed. Through dynamic analysis of the log i–log v plot (peak current (i_p) *vs.* scan rate (v)), it is found that the conversion process is mainly a redox reaction controlled by diffusion and capacitance. The fitted b values of two pairs of cathode and anode peaks are 0.93, 0.86, 0.90 and 0.99, respectively (Fig. S5). It indicates hybrid diffusion-capacitive control with rapid charge-carrier diffusion, thus enabling superior rate capability.[27] The contributions of surface-controlled capacitances were quantified using $i = k_1v + k_2v^{1/2}$, where k_1v and $k_2v^{1/2}$ represent capacitive and diffusion-controlled components. The results show that at scan rates of 0.1, 0.2, 0.4, 0.6, 0.8, and 1.0 mV s^{-1}, the surface-controlled capacitance contribution rates are 77%, 78%, 84%, 88%, 89%, and 91%, respectively. Compared with the HCl-modified electrolyte at an equivalent concentration, $ZnSO_4$/LLH exhibits higher capacitance contribution (Fig. 2b and S6), indicating its improved rate performance and fast reaction kinetics of the $2I^-/I_2^0/2I^+$ conversion

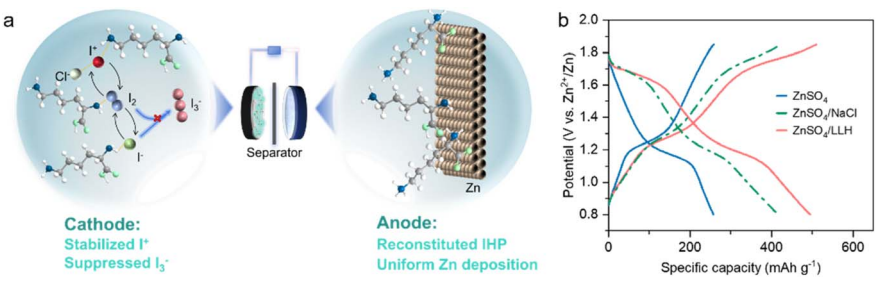

Fig. 1 Activating and stabilizing $2I^-/I_2^0/2I^+$ redox conversion of Zn||I_2 batteries with electrolyte additive LLH. (a) Schematic diagram of the working mechanism. (b) Galvanostatic charge–discharge behaviors in different electrolytes.

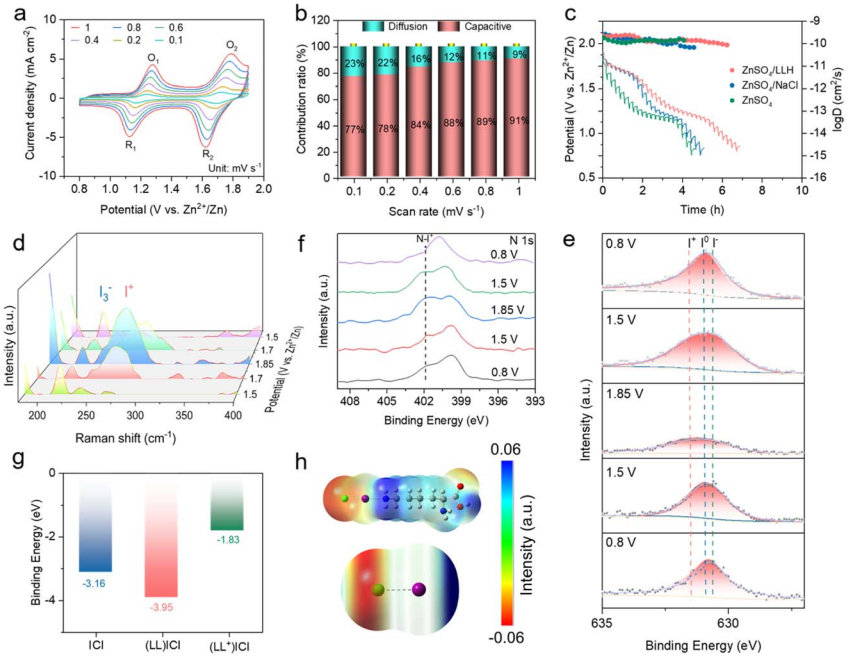

Fig. 2 Four-electron $2I^-/I_2^0/2I^+$ conversion mechanism of Zn||I_2 batteries in $ZnSO_4$/LLH electrolytes. (a) CV curves at different scan rates. (b) Contribution ratios of surface-controlled and diffusion-controlled capacities derived from fitting analysis at different scan rates. (c) GITT profiles and the corresponding diffusion coefficients of Zn||I_2 full batteries in different electrolytes.[26] (d) *In situ* Raman spectroscopy of electrochemical processes. (e) *Ex situ* XPS spectra of I 3d for the cathode at different potentials during charge/discharge. (f) High-resolution N 1s spectra of the I_2 cathode at different voltages. (g) The different coordination forms of fixed I^+ and the corresponding binding energies. (h) Electrostatic potential of (LL)ICl (top) and ICl (bottom) (green spheres: Cl^-, purple spheres: I^+).

process. Galvanostatic intermittent titration technique (GITT) measurements revealed high ion diffusion coefficients (approximately 10^{-9} to 10^{-12} cm^2 s^{-1}) in the LLH-modified electrolyte (Fig. 2c).[26,28] Diffusion coefficients during discharge are typically lower than those during charge, indicating that the I_2^0 to $2I^-$ conversion proceeds faster than the $2I^+$ to I_2^0 conversion. This kinetic behavior is consistent with cyclic voltammetry (CV) analysis.

Subsequently, *in situ* Raman spectroscopy was employed to investigate the four-electron ($2I^-/I_2^0/2I^+$) conversion mechanism. A peak at 216 cm^{-1}, assigned to I_3^-, weakens upon charging to 1.7 V, while a peak at 265 cm^{-1}, corresponding to I^+, intensified with increasing voltage (Fig. 2d). These observations confirm successful I^+ anchoring. During discharge, the I^+ peak diminishes as the voltage decreased, indicating reversible $2I^-/I_2^0/2I^+$ redox transitions. The X-ray photoelectron spectroscopy (XPS) analysis of cathodes at varying potentials reveals a gradual increase in binding energy during charging and a decrease during discharging (Fig. 2e and S7). This aligns with a valence state evolution during charging ($2I^- \rightarrow I_2^0 \rightarrow 2I^+$) and the reverse during discharging ($2I^+ \rightarrow I_2^0 \rightarrow 2I^-$), demonstrating the reversibility of $2I^-/I_2^0/2I^+$ redox reactions and effective I^+ stabilization. Subsequently, further analysis of the 1s orbital of N reveals the appearance of an additional peak shape after charging to 1.85 V, which gradually disappears during discharge. This is speculated to be due to the coordination between N and I^+ of LLH during charging, which also serves as an anchoring mechanism (Fig. 2f).[29] DFT calculation results reveal that the (LL)ICl coordination mode possesses the highest binding energy, indicating the superior stability of this bidentate structure of ICl (Fig. 2h and S8). This configuration anchors I^+ more effectively against hydrolysis compared to monodentate ICl coordination. Experimental observations correlate with these findings, where HCl-modified full batteries underperform LLH-based counterparts. Monodentate coordination enables four-electron reactions but provides inferior I^+ anchoring capability relative to the (LL)ICl bidentate structure. Partial protonation occurs in the electrolyte, generating protonated L-lysine (LL^+) species. Electrostatic interactions between LL^+ and ICl_2^- constitute an alternative I^+ anchoring mechanism. Calculated binding energies for this configuration remain comparatively low, suggesting limited stability. Electrostatic potential distributions demonstrate simultaneous I^+ anchoring by N and Cl atoms (Fig. 2g). The (LL)ICl bidentate coordination thus establishes a stable I^+ interaction mechanism, achieving enhanced theoretical specific capacity.

Moreover, *in situ* UV-vis spectroscopy further reveals two characteristic I_3^- peaks at 287 nm and 350 nm in $ZnSO_4$ electrolytes upon charging to 1.2 V.[30] The peak intensities increase with voltage (Fig. 3a), indicating continuous formation, accumulation, and diffusion of I_3^- from the cathode during cycling. Conversely, these peaks are significantly suppressed in $ZnSO_4$/LLH, becoming nearly undetectable under identical conditions (Fig. 3b). Minimal intensity increase above 1.6 V demonstrates that LLH enhances reaction kinetics and suppresses polyiodide shuttling.[31] Theoretical calculations elucidated interactions

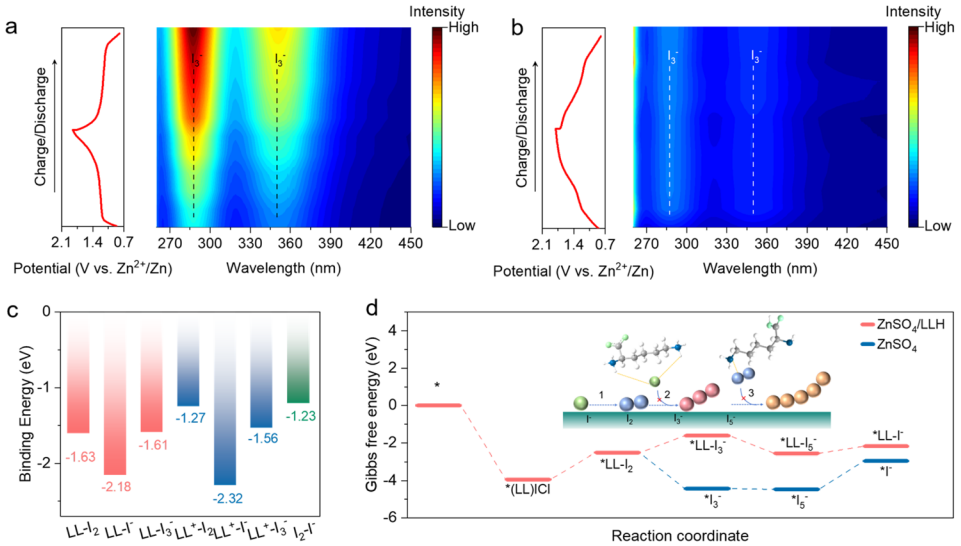

Fig. 3 Interactions of LLH with iodine species. (a and b) *In situ* UV-vis spectra of Zn||I_2 batteries in 2 M $ZnSO_4$ electrolytes without/with LLH. (c) Adsorption energy of LL toward I^-, I_2, and I_3^- species. Binding energies are represented by red (LL-iodine species), blue (LL^+-iodine species) and green (I_2–I^- interaction), respectively. (d) The Gibbs free energy profiles for I^+ reduction in different electrolytes.

between the LL/LL^+ and iodine species (I^-, I_2, I_3^-). Computational results reveal substantially reduced binding energy between both LL/LL^+ and I^-, indicating the preferential adsorption of I^- towards LL^+ among iodine species (Fig. 3c and S9). This I^-–LL^+ interaction (physical adsorption) during discharge suppresses the bonding between newly formed I^- and residual I_2, thereby inhibiting I_3^- formation at the cathode. Gibbs free energy profiles for iodine reduction reactions were computed, where the energy decrease (−3.95 eV) for the $I^+ \rightarrow$ (LL)ICl transition demonstrates strong spontaneity and structural stability (Fig. 3d).[25,32] Notably, LLH addition increased ΔG values for $I_2 \rightarrow I_3^-$ conversion, indicating non-spontaneous reaction characteristics. Concurrently, reduced ΔG values for $I_5^- \rightarrow I^-$ were observed relative to the $ZnSO_4$ electrolyte, suggesting facilitated polyiodide conversion to I^-. These results validate LLH's dual functionality: effective I^+ anchoring and suppression of the shuttle effect.

Protection of the zinc anode by the LLH-optimized electrolyte

A comprehensive investigation combining DFT calculations and electrochemical characterization was conducted to assess the interfacial stabilization effects of LLH on zinc anodes. Zn||Zn symmetric battery configurations with controlled LLH concentration gradients were employed for electrochemical analysis. The symmetric battery with 500 mM LLH in the electrolyte exhibits an enhanced cycling stability of 900 h at 5 mA cm^{-2}, 2.5 mAh cm^{-2}. The symmetric battery with $ZnSO_4$/LLH electrolyte promotes smooth, uniform Zn deposits, indicating preferential (002)-oriented deposition, and suppresses corrosion/side reactions (Fig. 4a and S10). In contrast, the scanning electron microscopy (SEM) images of Zn anodes cycled for 50 h at 1 mA cm^{-2} and 1 mAh cm^{-2} reveal rough surfaces with dendrites, dead Zn fragments, and irregular by-products in $ZnSO_4$ (Fig. 4b and S10). These features reduce the active surface area, degrade cycling stability and provide more reaction sites for further corrosion and side reactions. Chronoamperometry at −150 mV overpotential reveals a current density of ~23.5 mA cm^{-2} after 500 s in $ZnSO_4$, corresponding to 2D diffusion-driven Zn^{2+} aggregation and dendrite growth. In $ZnSO_4$/LLH, the Zn^{2+} kinetics exhibits rapid transition to 3D diffusion with reduced current density (Fig. 4c). Linear sweep voltammetry (LSV) was subsequently employed to evaluate the electrochemical stability window, revealing that LLH incorporation suppresses the HER and oxygen evolution reaction (OER), while broadening the electrochemical stability window from −0.15 to 2.5 (V *vs.* Zn^{2+}/Zn) (Fig. 4d, S11 and S12). This enhancement improves electrolyte stability during deposition/stripping cycles. In addition, CV tests on Zn||Ti batteries were conducted to evaluate the nucleation potential of Zn. The nucleation overpotential in $ZnSO_4$/LLH electrolyte (19.0 mV) is lower than that in $ZnSO_4$/LLH electrolyte (36.5 mV) (Fig. 4e). These results demonstrate that LLH mitigates parasitic reactions (*e.g.*, HER and passivation) and enables homogeneous Zn^{2+} deposition, effectively suppressing dendrite formation.

IHP reconstruction consequently emerges as a principal strategy for optimizing zinc anode reversibility through interfacial engineering. Electrical double layer (EDL) capacitance measurements reveal a lower value for $ZnSO_4$/LLH (96.38 μF cm^{-2}) compared to $ZnSO_4$ (130.91 μF cm^{-2}), indicating LL adsorption at the Zn surface and IHP restructuring (Fig. 4f and S13).[33] Molecular orbital analysis shows the highest occupied molecular orbital (HOMO) of LL^+ (−0.351 eV) and LL (−6.544 eV) is higher than that of H_2O (−8.701 eV), and the lowest unoccupied molecular orbital (LUMO) of LL^+ (−0.205 eV) and LL (−0.473 eV) is lower, favoring electron transfer to zinc surfaces, thereby promoting LL^+ adsorption (Fig. S14). This reduces the H_2O molecule population density within the IHP, inducing IHP structural reconfiguration. Contact angle

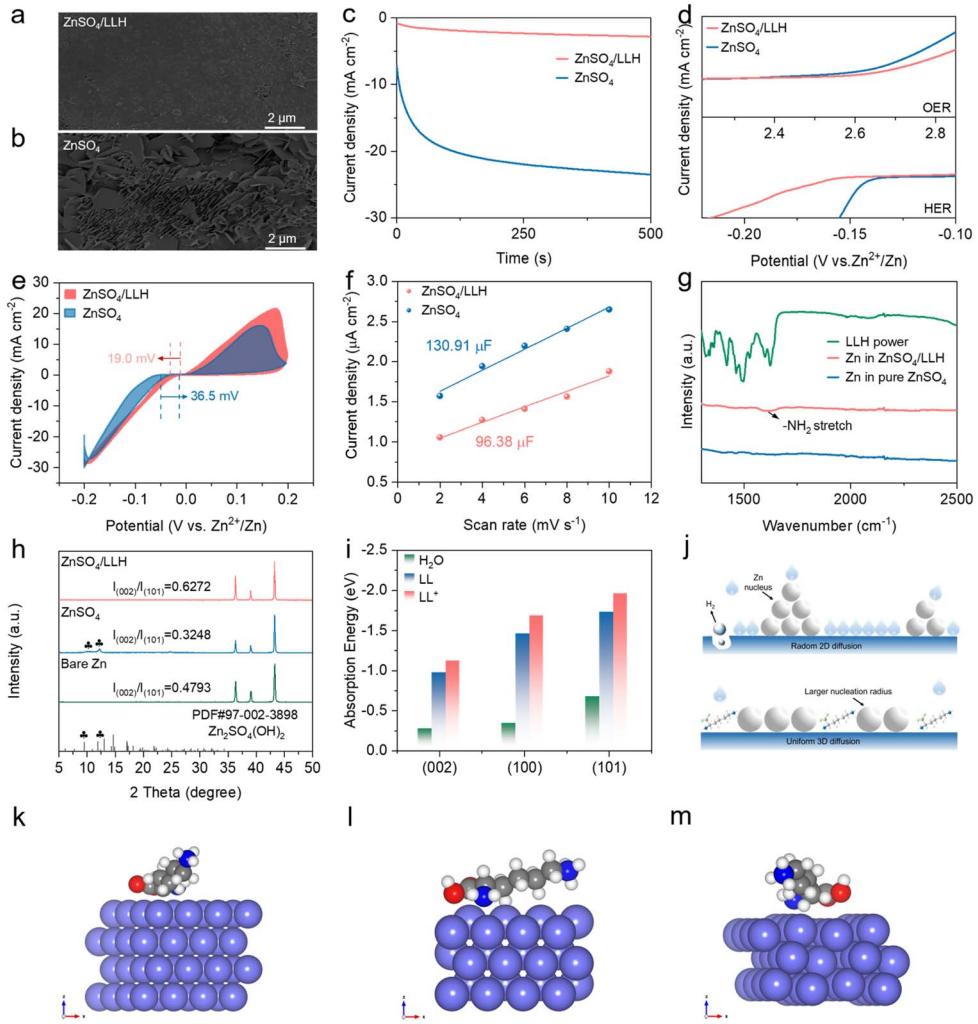

Fig. 4 Comparison of $ZnSO_4$/LLH and $ZnSO_4$ electrolytes on zinc anode performance. (a and b) SEM images of Zn anode surfaces during the deposition in Zn||Zn symmetric batteries at 1 mA cm^{-2}, 1 mAh cm^{-2}. (c) Chronoamperometry of Zn metal. (d) Hydrogen evolution potential measurement with Zn||Zn symmetric batteries and oxygen evolution potential measurement with Zn||Ti batteries. (e) CV curves of Zn nucleation on Ti at a scan rate of 1 mV s^{-1}. (f) EDL capacitance of the Zn substrate. (g) FTIR spectra of Zn foil after immersion in electrolytes and LLH powder. (h) The XRD pattern of zinc foil after 50 cycles at 1 mA cm^{-2}, 1 mAh cm^{-2}. (i) Adsorption energies of LL, LL^+, and water molecules on different Zn crystal planes. (j) Schematic of the EDL structure. The optimized adsorption configurations of LL^+ on different Zn crystal planes: (k) (002), (l) (100), and (m) (101).

measurements also demonstrate improved wettability in $ZnSO_4$/LLH (from 84° to 92°, Fig. S15), indicating enhanced zincophilic properties for uniform ion transport. LL^+ alignment in the IHP suppresses H_2O mobility/activity, mitigates parasitic reactions, and directs Zn^{2+} deposition *via* electronegative functional groups.[34]

The FTIR analysis of Zn foils soaked in $ZnSO_4$/LLH reveals a bending vibration peak assigned to amino groups at 1600 cm^{-1}, while the Zn foil immersed in $ZnSO_4$ did not exhibit this peak, confirming LL^+ surface adsorption (Fig. 4g). In addition, comparative energy-dispersive spectroscopy (EDS) mapping of zinc foils immersed in both electrolytes for 15 days reveals the homogeneous distribution of C, N, and O elements on $ZnSO_4$-LLH immersed foils, confirming uniform LL^+ adsorption (Fig. S16 and S17). In contrast, EDS mapping reveals spatially overlapping S, O, and Zn signals on zinc surfaces in pure $ZnSO_4$ electrolyte. These observations, combined with XRD analysis after 15 day immersion, confirm the formation of the $Zn_4SO_4(OH)_6 \cdot xH_2O$ byproduct (Fig. S18). LL^+ incorporation attenuates H_2O reactivity and reduced SO_4^{2-} population within IHP, thereby preserving zinc anode integrity.

The XPS results provide additional evidence for the interfacial interaction between LL^+ and the zinc metal surface. As shown in Fig. S19, the post-immersion zinc substrate exhibits distinct characteristic peaks in the high-resolution C 1s spectrum, corresponding to O–C=O (531.2 eV) and C–N/C–C (284.8 eV) functional groups derived from LL^+. Concurrently, the O 1s spectrum reveals prominent peaks associated with O–H (532.1 eV) and O–C=O (533.5 eV) species. These spectral features are absent in the bare zinc control samples. The O–C=O peak exhibits a binding energy shift to 532.1 eV, indicative of carboxyl group adsorption on the Zn surface which reduces local

electron density. XPS analysis reveals interfacial N–Zn bonding (399.4 eV) alongside LL^+'s native N–C peak (398.2 eV), demonstrating nitrogen-mediated chemisorption on zinc.

XRD analysis of Zn anodes was further carried out to elucidate the stabilizing effect of LLH on zinc anode morphology. Comparative XRD patterns of cycled Zn anodes of Zn||Zn symmetric batteries in different electrolytes reveal increased $I_{(002)}/I_{(100)}$ and $I_{(002)}/I_{(101)}$ ratios in the $ZnSO_4$/LLH electrolyte, demonstrating LLH-induced preferential (002)-oriented Zn deposition (Fig. 4h). DFT calculations were subsequently performed for verification, determining adsorption energies of H_2O, LL, and LL^+ on distinct zinc crystal facets. Both LL and LL^+ exhibited consistently more negative adsorption energies than H_2O on the (002), (100) and (101) planes, indicating stronger interactions with zinc metal anodes compared to water molecules, particularly for LL^+ (Fig. 4i, S20 and S21). Competitive adsorption displaces H_2O from zinc anode surfaces by LL^+ molecules, forming a hydration-depleted IHP. LL^+ cations are preferentially adsorbed onto the zinc surface, covering the high-charge-density active sites (*e.g.*, tips and defects) that are susceptible to rapid Zn^{2+} deposition and subsequent dendrite formation. This preferential adsorption redirects Zn^{2+} deposition toward regions with sparser LL^+ coverage and a more uniform electric field, thereby effectively suppressing zinc dendrite growth. This configuration suppresses parasitic reactions, while preferential adsorption hinders the lateral diffusion of Zn^{2+}, thereby restricting dendritic formation (Fig. 4j). The nuclear magnetic resonance spectra reveal that the ^2H peak of pure D_2O at 4.69 ppm shifts to 4.721 ppm after the addition of 2 M $ZnSO_4$, confirming strong Zn^{2+}–D_2O coordination. No significant peak shifts are observed with LLH addition, indicating LLH does not engage in solvation (Fig. S22).[35] FTIR spectroscopy corroborates these findings, showing no notable shifts in SO_4^{2-} vibrational bands, further confirming the absence of LLH-solvation interactions (Fig. S23).

Improved cycling performance with the LLH-optimized electrolyte

The pH stability of the electrolyte in ZIBs plays a critical role in suppressing zinc dendrite formation, mitigating the HER and enhancing cycling lifespan. Real-time monitoring of interfacial pH variations at the working electrode during charge/discharge was conducted using a custom-built *in situ* pH measurement system (Fig. S24). The addition of LLH results in attenuated pH fluctuations throughout the deposition/stripping cycles, with reduced pH variations observed before and after potential transitions at zinc foil interfaces. A substantial pH elevation occurs in $ZnSO_4$ electrolyte during zinc deposition due to the vigorous HER. Subsequent pH fluctuations stem from dynamic changes in local H^+ concentration at reaction sites. The initial pH rise during zinc stripping originates from the dissolution of the passivation layer formed during deposition, followed by gradual pH decrease induced by Zn^{2+} hydrolysis. The $ZnSO_4$/LLH electrolyte exhibits considerably attenuated pH variations throughout deposition/stripping cycles, demonstrating pH buffering capacity and HER suppression (Fig. 5a). This mechanism arises from lysine adsorption reducing the population of active water molecules at the IHP, thereby suppressing the HER. As an amphoteric amino acid, LLH contains α-carboxyl, α-amino, and ε-amino side chain groups. In weakly acidic electrolytes, the carboxyl groups undergo partial deprotonation to release H^+ while amino groups coordinate protons. Elevated pH triggers the deprotonation of –COOH and protonated amino groups to replenish H^+ concentration. Under acidic conditions, $-COO^-$ groups and amino functionalities sequester H^+ through protonation, establishing pH buffering capacity (Fig. S26). LLH can buffer the pH fluctuations induced by electrode reactions during charge/discharge cycles, thereby mitigating their impact on the bulk electrolyte pH. This effect reduces the occurrence of the HER and suppresses the formation of byproducts such as $Zn_4SO_4(OH)_6 \cdot xH_2O$.

Linear polarization measurements show a positive shift in corrosion potential for $ZnSO_4$/LLH (−0.966 V *vs.* Ag/AgCl) compared to pure $ZnSO_4$ (−0.972 V *vs.* Ag/AgCl), indicating enhanced thermodynamic stability. The corrosion current density decreases from 13.18 mA cm^{-2} to 8.13 mA cm^{-2}, confirming improved corrosion resistance. These findings suggest that LLH-mediated modification of the IHP effectively mitigates zinc anode corrosion (Fig. 5b).[36]

A comprehensive series of electrochemical evaluations was conducted to assess the synergistic effects of LL^+ at the IHP on zinc anode reversibility and stability. Zn||Zn symmetric batteries were subjected to varied current densities and areal capacities as primary evaluation parameters. As shown in Fig. 5c, batteries with the $ZnSO_4$ electrolyte exhibit irreversible voltage drops after 550 hours under 3 mA cm^{-2} and 1 mAh cm^{-2}, attributed to separator penetration by dendrite growth causing electrical shorting. In contrast, $ZnSO_4$/LLH electrolyte-based batteries demonstrate extended cycling stability exceeding 4000 hours. This behavior originates from LL^+ adsorption at the interface, which facilitates Zn^{2+} transport kinetics and promotes uniform zinc deposition. $ZnSO_4$/LLH electrolyte batteries exhibited stable cycling for over 2850 hours at 5 mA cm^{-2} and 1 mAh cm^{-2}, as well as 2250 hours at 1 mA cm^{-2} under identical capacity conditions (Fig. S27 and S28). Comparative analysis across current densities reveals enhanced cycling stability relative to pure $ZnSO_4$ electrolyte systems.

As shown in Fig. 5d, Zn||Zn symmetric batteries with pure $ZnSO_4$ electrolyte exhibit unstable potential hysteresis at 50 mA cm^{-2} and undergo rapid failure after 130 hours. This behavior originates from accelerated Zn^{2+} migration under high current density. However, sluggish deposition kinetics cause Zn^{2+} accumulation at the interface, impeding subsequent ion transport and inducing severe concentration polarization. Simultaneously, solvated water molecules associated with accumulated Zn^{2+} promote parasitic reactions, further exacerbating electrolyte/electrode interfacial instability. The $ZnSO_4$/LLH electrolyte demonstrates extended cycling stability exceeding 650 hours, attributed to accelerated reaction kinetics and ordered zinc deposition morphology. Reversibility analysis *via* symmetric batteries reveals superior rate capability and high reversibility for $ZnSO_4$/LLH-based Zn||Zn batteries across current densities from 1 to 50 mA cm^{-2} (Fig. 5e). This demonstrates enhanced compatibility of LLH-modified zinc-ion batteries with commercial fast-charging requirements of high-power charge/discharge capability.

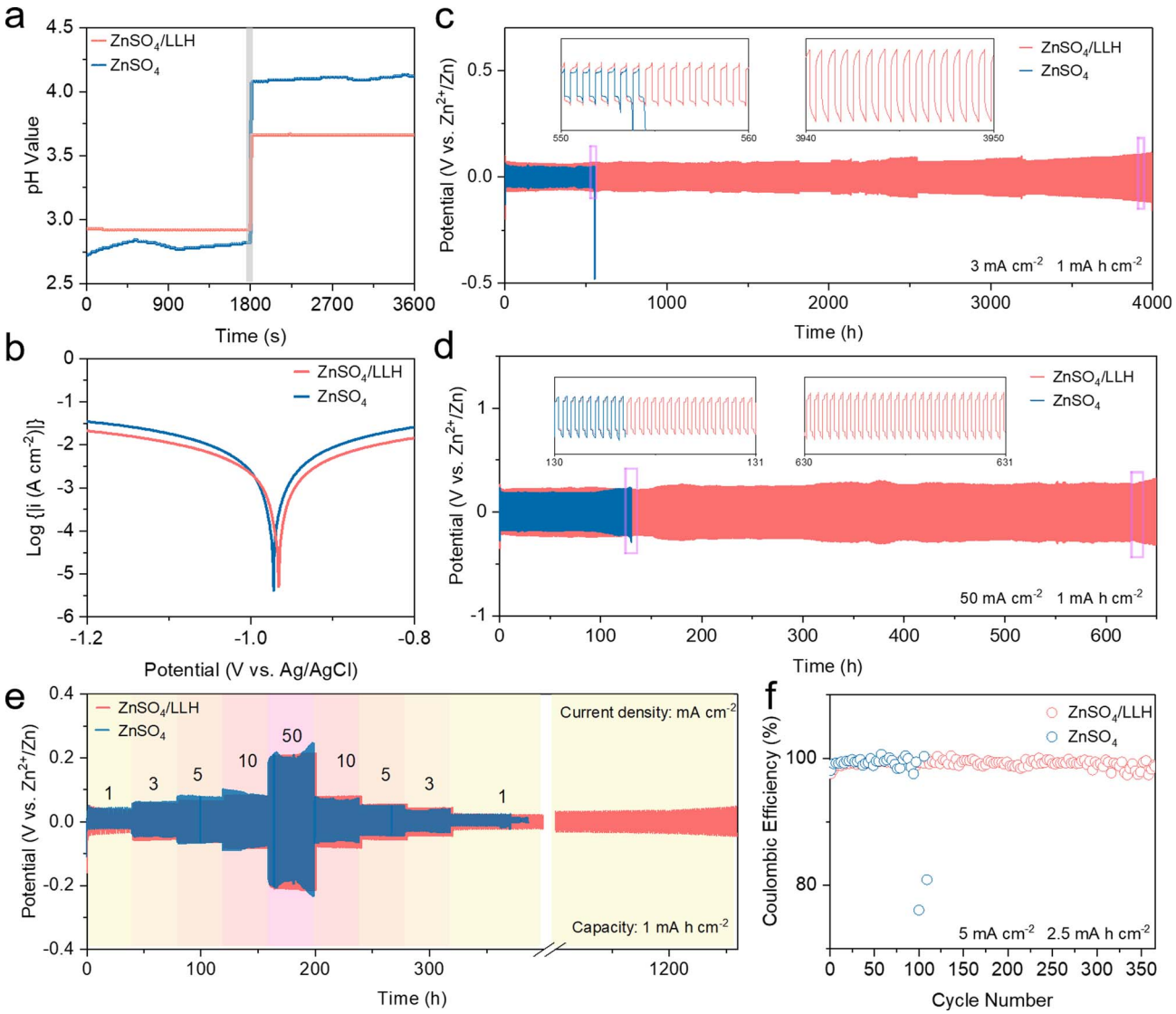

Fig. 5 Electrochemical reversibility and stability of the Zn foil anode in $ZnSO_4$/LLH and $ZnSO_4$ electrolytes. (a) *In situ* pH tests in Zn||Zn symmetric batteries. (b) Tafel plots. Galvanostatic voltage profiles of a Zn||Zn symmetric battery cycled for plating-stripping at (c) 3 mA cm^{-2}, 1 mAh cm^{-2} and (d) 50 mA cm^{-2}, 1 mAh cm^{-2}. (e) Rate performance of Zn||Zn symmetric batteries at various current densities. (f) The CE of Zn||Ti batteries at 5 mA cm^{-2}, 2.5 mAh cm^{-2}.

CE of Zn||Ti batteries in $ZnSO_4$ electrolyte deteriorates rapidly beyond 113 plating/stripping cycles under 5 mA cm^{-2} and 2.5 mAh cm^{-2} conditions during reversibility testing (Fig. 5f). Degradation correlates with dendritic-induced micro-shorts. The $ZnSO_4$/LLH electrolyte-based batteries demonstrate superior reversibility with stable cycling exceeding 350 cycles and an average CE of 99.2%. This improvement stems from LL^+-induced homogeneous Zn^{2+} distribution and uniform zinc deposition. Fig. S29 and S30 illustrate stable cycling performance exceeding 800 cycles at 1 mAh cm^{-2} under 2 mA cm^{-2} and 1000 cycles at 1 mAh cm^{-2} under 5 mA cm^{-2}, with average CE values of 98.8% and 99.4%, respectively. These performance metrics substantiate LL^+'s critical role in establishing interfacial conditions enabling long-term zinc metal anode stabilization through IHP-mediated homogeneous deposition.

Performance of Zn||I_2 full batteries

Full-battery evaluations were performed on four-electron transfer Zn||I_2 batteries employing $ZnSO_4$/LLH electrolyte. Rate capability across 1–15 A g^{-1} demonstrates specific capacities of 502, 472, 410, 362, 329, and 268 mAh g^{-1} for $ZnSO_4$/LLH-based batteries (Fig. 6a and S2). A maximum net specific capacity of 409 mAh g^{-1} is achieved. The capacity retention is significantly enhanced when the current density is restored to 1 A g^{-1}, delivering a specific capacity of 499 mAh g^{-1}. Galvanostatic charge–discharge profiles (Fig. 6b) exhibit two distinct voltage plateaus at various current densities, attributed to effective I^+ anchoring within the electrolyte. These values represent substantial capacity enhancement over pure $ZnSO_4$ systems, highlighting the efficacy of $2I^-/I_2^0/2I^+$ four-electron redox chemistry. Comparative analysis with $ZnSO_4$/HCl

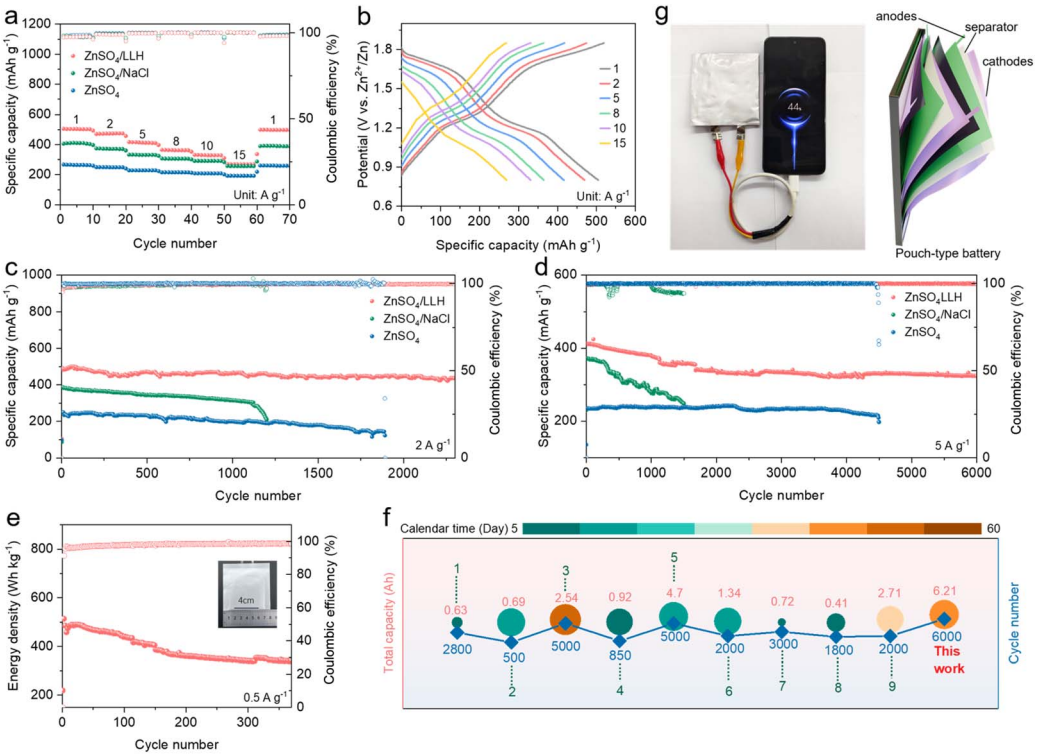

Fig. 6 Electrochemical performance of Zn||I_2 batteries in the LLH-optimized electrolytes. (a) Rate capacities at different current densities. (b) Galvanostatic charge–discharge curves under a wide range of current densities, ranging from 1 to 15 A g^{-1}. (c) Cycling stability at 2 A g^{-1}. (d) Cycling stability at 5 A g^{-1}. (e) Cyclic performance of the pouch batteries at 0.5 A g^{-1}. (f) Comparison of current research on iodine-based batteries based on the four-electron transfer mechanism. In addition to the two descriptors on left and right sides, the area of every circle qualitatively reflects the specific capacity of the battery, whereas the color index corresponds to the calendar time. (g) Demonstration of Zn||I_2 pouch batteries applied for mobile phone charging and schematic diagram of their series configuration.

electrolyte systems reveals superior specific capacity at equivalent concentrations, indicating the enhanced stability of I^+ and energy density provision by LLH *versus* HCl.

Pure $ZnSO_4$-based Zn||I_2 batteries exhibit capacity decay to 122.4 mAh g^{-1} after 1900 cycles at 2 A g^{-1}, caused by separator piercing due to anode dendrite formation. HCl-modified batteries display rapid capacity fade (53.64% retention) after 1200 cycles with 98.94% average CE. This degradation is attributed to continuous cathode active material loss *via* iodine species shuttling, combined with I_3^--mediated oxidation of zinc metal causing anode corrosion, which substantially reduces both specific capacity and CE. Furthermore, corrosion-induced anode surface heterogeneity disrupted subsequent uniform zinc deposition, while non-uniform electric field distribution triggered the HER and passivation. Additionally, competitive chlorine evolution reactions progressively depleted Cl^- anions during cycling, ultimately compromising I^+ stabilization capability, resulting in a 50% reduction in specific capacity. LLH-incorporating batteries exhibited 86.48% capacity retention (435.5 mAh g^{-1}) with an average CE of 99.4% after 2300 cycles (Fig. 6c). GCD curves for LLH-based systems (Fig. S31) exhibit stable $2I^+/I_2^0$ plateaus. The Zn||I_2 cell employing $ZnSO_4$/LLH electrolyte achieved 6000 cycles at a high current density of 5 A g^{-1}, retaining a discharge capacity of 323.9 mAh g^{-1} with a coulombic efficiency of 99.4%, which indicates dual stabilization of both the cathode and the zinc anode (Fig. 6d). The substantially enhanced cycling stability originates from LLH's superior I^+ anchoring capability, optimized iodine conversion kinetics, and dual suppression of zinc dendrites and parasitic reactions. Practical viability was demonstrated through 4 × 4 cm^2 pouch batteries employing $ZnSO_4$/LLH electrolyte, which sustains 350 stable cycles at 0.5 A g^{-1} (Fig. 6e). Comparative analysis with prior Zn||I_2 systems demonstrates the superior performance of LLH-modified Zn||I_2 batteries in specific capacity and cycling stability among other parameters (Fig. 6f).[23,25,27,29,37–42] Pouch batteries were subsequently evaluated under various operational conditions, where a single 4 × 4 cm^2 battery powered a miniature fan and retained functionality after 180° bending deformation and mechanical restoration (Fig. S32). A series-connected array of three identical pouch batteries successfully powered a mobile device, as shown in Fig. 6g.

Conclusions

In summary, incorporating cost-effective LLH as an additive effectively enhances the performance of aqueous ZIBs. Spectroscopic characterization and theoretical simulations reveal LLH stabilizes intermediate I^+ species. This enables a highly reversible four-electron redox conversion ($2I^-/I_2^0/2I^+$), which enhances the specific capacity by 89%. Moreover, the functional groups of LLH suppress the iodine shuttle effect by interacting

with I_2 and I^-. In addition, LL^+ adsorption on the zinc anode surface restructures the IHP, promoting homogeneous zinc deposition and mitigating side reactions such as corrosion and passivation. This improves deposition reversibility, extending the anode's cycle life beyond 4000 hours. The synergistic modification of both electrodes results in outstanding overall performance: a high specific capacity of 502 mAh g^{-1} at 1 A g^{-1}. Additionally, a practical 4 × 4 cm^2 pouch cell demonstrates stable operation for over 350 cycles at 0.5 A g^{-1}.

Author contributions

H. Zhang designed and conducted the experiments, performed the data analysis, and drafted the manuscript; X. Zhang assisted with data discussion and analysis; D. Ma, X. Cai, M. Lv, and H. Yan participated in the data discussion and analysis; Junbo Niu participated in the theoretical calculation work; W. Song conceived and supervised the research, and contributed to methodology development, manuscript revision, and funding acquisition.

Conflicts of interest

There are no conflicts to declare.

Data availability

The data supporting this article have been included as part of the supplementary information (SI). Supplementary information: materials and experimental details, characterisation data, and electrochemical performance data (Fig. S1–S32 and, Tables S1 and S2). See DOI: https://doi.org/10.1039/d6sc00182c.

Acknowledgements

This work was financially supported by the National Natural Science Foundation of China (No. 22172103).

References

1 Y. Li, M. Zhang, H. Lu, X. Cai, Z. Jiao, S. Li and W. Song, Boosting High-Performance Aqueous Zinc-Ion Hybrid Capacitors via Organic Redox Species on Laser-Induced Graphene Network, *Adv. Funct. Mater.*, 2024, **34**, 2400663.

2 Y. Li, H. Ba, Z. Wang, S. Wu, Y. Shang, S. Huang and H. Y. Yang, Electrolyte pH and operating potential: critical factors regulating the anodic oxidation and zinc storage mechanisms in aqueous zinc ion battery, *Mater. Today Energy*, 2024, **39**, 101460.

3 J. Tao, X. Cai, Y. Li, L. Huang, X. Zhang, H. Zhang, D. Ma, L. Ran and W. Song, A Synergistic Zincophilic and Hydrophobic Supramolecule Shielding Layer for Actualizing Long-Term Zinc-Ion Batteries, *Adv. Energy Mater.*, 2025, **15**, 2403662.

4 T. Xiao, J.-L. Yang, D. Chao and H. J. Fan, Multimodal electrolyte architecting for static aqueous zinc-halogen batteries, *Natl. Sci. Rev.*, 2025, **12**, nwaf029.

5 F. Bu, Z. Sun, W. Zhou, Y. Zhang, Y. Chen, B. Ma, X. Liu, P. Liang, C. Zhong, R. Zhao, H. Li, L. Wang, T. Zhang, B. Wang, Z. Zhao, J. Zhang, W. Li, Y. S. Ibrahim, Y. Hassan, A. Elzatahry, D. Chao and D. Zhao, Reviving Zn0 Dendrites to Electroactive Zn^{2+} by Mesoporous MXene with Active Edge Sites, *J. Am. Chem. Soc.*, 2023, **145**, 24284–24293.

6 Y. Su, B. Chen, Y. Sun, Z. Xue, Y. Zou, D. Yang, L. Sun, X. Yang, C. Li, Y. Yang, X. Song, W. Guo, S. Dou, D. Chao, Z. Liu and J. Sun, Rationalized Electroepitaxy toward Scalable Single-Crystal Zn Anodes, *Adv. Mater.*, 2023, **35**, 2301410.

7 R. Hao, S. Gu, Z. Wang, J. Chen, W. Luo, J. Hu, C. Yan, H. Yuan, G. Liu, K. Liu, C. Liu, W. Wang and Z. Lu, Reconstructing the solvation structure and solid-liquid interface enables dendrite-free zinc-ion batteries, *Mater. Today Energy*, 2023, **33**, 101279.

8 G. Li, Q. Cai, S. Zhang, J. A. Yuwono, L. Mao, H. Jin and Z. Guo, Decoupled dual-salt electrolyte for practical aqueous zinc batteries, *Nat. Sustain.*, 2025, **8**, 1349–1359.

9 X. Liang, Q. Dong, S. Guo, C. Zeng, Z. Chen, B. Zhang, C. Zhou, J. Zhang, Z. Xing, X. Tian and X. Shi, Customized Design of R-SO3H-Containing Binders for Durable Iodine-Loading Cathode of Zinc–Iodine Batteries, *Adv. Energy Mater.*, 2025, **15**, 2500673.

10 X. Cai, X. Wang, Z. Bie, Z. Jiao, Y. Li, W. Yan, H. J. Fan and W. Song, A Layer-by-Layer Self-Assembled Bio-Macromolecule Film for Stable Zinc Anode, *Adv. Mater.*, 2024, **36**, 2306734.

11 X. Fu, Y. Pan, Z. Chen, F. Li, Y. Yang, M. Chen, H. Tu, T. Qiu, Z. Xing, P. Rao, Z. Kang, W. Zhang, X. Shi, L. Shan and X. Tian, Amino acid-based functional additive enables fast polyiodide conversion kinetics for durable Zn-I_2 batteries, *Energy Environ. Sci.*, 2026, DOI: 10.1039/D5EE06668A.

12 X. Chen, D. Feng, Y. Jiao and P. Wu, Dual-Electrode Synergistic Electrolyte Enabling Highly Reversible Multi-Electron Redox in Aqueous Zinc-Iodine Batteries, *Adv. Mater.*, 2025, e13389.

13 H. Ge, X. Feng, D. Liu and Y. Zhang, Recent advances and perspectives for Zn-based batteries: Zn anode and electrolyte, *Nano Res. Energy*, 2023, **2**, e9120039.

14 M. Zhu, X. Li, W. Ni, C. Cai, J. Zhong, M. Zhong, L. Huang, Y. Tian and J. Zhang, Manipulating oriented crystal growth of Zn via lattice-matched and zincophilic MXene nanoarrays towards dendrite-free Zn batteries, *J. Colloid Interface Sci.*, 2025, **691**, 137433.

15 J. Wu, J.-L. Yang, B. Zhang and H. J. Fan, Immobilizing Polyiodides with Expanded Zn^{2+} Channels for High-Rate Practical Zinc-Iodine Battery, *Adv. Energy Mater.*, 2024, **14**, 2302738.

16 C. Xu, C. Lei, P. Jiang, W. Yang, W. Ma, X. He and X. Liang, Practical high-energy aqueous zinc-bromine static batteries enabled by synergistic exclusion-complexation chemistry, *Joule*, 2024, **8**, 461–481.

17 X. He, X.-Y. Kong and L. Wen, A promising solution for highly reversible zinc metal anode chemistry: Functional gradient interphase, *Nano Res. Energy*, 2024, **3**, e9120100.

18 P. Jiang, Q. Du, C. Lei, C. Xu, T. Liu, X. He and X. Liang, Stabilized four-electron aqueous zinc–iodine batteries by quaternary ammonium complexation, *Chem. Sci.*, 2024, **15**, 3357–3364.

19 H. Zhao, L. Zhao, D. Yin, N. Gao, Y. Zhang, J. Feng, X. Chen, X. Liu, J. Wei, C. Fan, G. Gao, C. Xiao and S. Ding, Key Issues and Strategies in Aqueous Static Zinc–Halogen Battery Design, *Adv. Mater.*, 2025, e15759.

20 Z. Shi, G. Liu, H. Huang, Z. He, C. Lei, Z. Feng, M. Ye, Y. Zhang, Z. Wen, W. Du, X. Liu, Y. Wei, Q. Yang, Y. Tang and C. C. Li, Coordination-escorted organo-interhalogen conversion enables durable dual-deposition Zn‖I_2 batteries with high areal capacities, *Energy Environ. Sci.*, 2026, DOI: 10.1039/D5EE06160A.

21 K. Chen, Y. Xu, H. Li, Y. Li, L. Zhang, Y. Guo, Q. Xu, Y. Li and H. Xie, Design of cellulosic poly(ionic liquid)s with a hydrogen bond/ion dual regulation mechanism for highly reversible Zn anodes, *Chem. Sci.*, 2025, **16**, 8648–8660.

22 T. Liu, C. Lei, H. Wang, J. Li, P. Jiang, X. He and X. Liang, Aqueous Electrolyte With Weak Hydrogen Bonds for Four-Electron Zinc–Iodine Battery Operates in a Wide Temperature Range, *Adv. Mater.*, 2024, **36**, 2405473.

23 X. Li, Y. Wang, Z. Chen, P. Li, G. Liang, Z. Huang, Q. Yang, A. Chen, H. Cui, B. Dong, H. He and C. Zhi, Two-Electron Redox Chemistry Enabled High-Performance Iodide-Ion Conversion Battery, *Angew. Chem., Int. Ed.*, 2022, **61**, e202113576.

24 Y. Zou, T. Liu, Q. Du, Y. Li, H. Yi, X. Zhou, Z. Li, L. Gao, L. Zhang and X. Liang, A four-electron Zn-I_2 aqueous battery enabled by reversible $I^-/I_2/I^+$ conversion, *Nat. Commun.*, 2021, **12**, 170.

25 W. Li, H. Xu, H. Zhang, F. Wei, T. Zhang, Y. Wu, L. Huang, J. Fu, C. Jing, J. Cheng and S. Liu, Designing ternary hydrated eutectic electrolyte capable of four-electron conversion for advanced Zn–I_2 full batteries, *Energy Environ. Sci.*, 2023, **16**, 4502–4510.

26 J. Hu, Z. Zhang, T. Deng, F. C. Cui, X. Shi, Y. Tian and G. Zhu, Porous Aromatic Frameworks Enabling Polyiodide Confinement toward High Capacity and Long Lifespan Zinc–Iodine Batteries, *Adv. Mater.*, 2024, **36**, 2401091.

27 X. Li, S. Wang, D. Zhang, P. Li, Z. Chen, A. Chen, Z. Huang, G. Liang, A. L. Rogach and C. Zhi, Perovskite Cathodes for Aqueous and Organic Iodine Batteries Operating Under One and Two Electrons Redox Modes, *Adv. Mater.*, 2023, **36**, 2304557.

28 Z. Lian, W. Yang, Z. Wu, L. Zhong, Z. Liu, Z. Chen, G. Lian, E. Iwuoha, K. Ocakoglu, J. Lu, S. Zhang, G. Zhou and X. Peng, A Diffusion-Retarded Strategy for Practical Zn–I_2 Batteries Under Harsh Conditions, *Angew. Chem., Int. Ed.*, 2026, **65**, e15756.

29 M. Wang, Y. Meng, M. Sajid, Z. Xie, P. Tong, Z. Ma, K. Zhang, D. Shen, R. Luo, L. Song, L. Wu, X. Zheng, X. Li and W. Chen, Bidentate Coordination Structure Facilitates High-Voltage and High-Utilization Aqueous Zn–I_2 Batteries, *Angew. Chem., Int. Ed.*, 2024, **63**, e202404784.

30 Y. Wang, X. Jin, J. Xiong, Q. Zhu, Q. Li, R. Wang, J. Li, Y. Fan, Y. Zhao and X. Sun, Ultra-stable Electrolytic Zn-I_2 Batteries Based on Nanocarbon Wrapped by Highly Efficient Single-Atom Fe-NC Iodine Catalysts, *Adv. Mater.*, 2024, **36**, 2404093.

31 H. Chen, X. Li, K. Fang, H. Wang, J. Ning and Y. Hu, Aqueous Zinc-Iodine Batteries: From Electrochemistry to Energy Storage Mechanism, *Adv. Energy Mater.*, 2023, **13**, 2302187.

32 L. Ran, X. Cai, D. Ma, J. Zhao, H. Zhang, S. Liang, J. Tao, X. Zhang, Y. Li, H. J. Fan and W. Song, Stable Four-Electron Zinc-Iodine Battery Realized by Polyacrylamide as Catalytic Binder, *Angew. Chem., Int. Ed.*, 2025, **64**, e15918.

33 X. Ma, Q. Wang, X. Zhang, Y. Lin, F. Zhang, J. Huang and Y. Wang, Highly reversible zinc anode enabled by a trace-amount additive with pH buffering capability, *Energy Environ. Sci.*, 2025, **18**, 982–990.

34 R. Jiang, T. Naren, Y. Chen, Z. Chen, C. Zhang, Y. Xie, L. Chen, Y. Qi, Q. Meng, W. Wei and L. Zhou, Enhanced Hydrogen Bonding Through Strong Water-Locking Additives for Long-Term Cycling of Zinc Ion Batteries, *Adv. Funct. Mater.*, 2024, **34**, 2411477.

35 N. Hu, W. Lv, W. Chen, H. Tang, X. Zhang, H. Qin, D. Huang, J. Zhu, Z. Chen, J. Xu and H. He, A Double-Charged Organic Molecule Additive to Customize Electric Double Layer for Super-Stable and Deep-Rechargeable Zn Metal Pouch Batteries, *Adv. Funct. Mater.*, 2024, **34**, 2311773.

36 Y. Wu, M. Xie, K. Fu, Z. Li, H. Shi, J. Zhang, L. Wang, Y. Jiang, C. Liu, D. Ma, H. Huang, F. Zeng, Y. Liao, H. Liu, Y. Ren and X. Liang, Realizing Lean-Electrolyte Zinc-Ion Batteries via An Ultrathin and Cost-Effective Separator, *Adv. Funct. Mater.*, 2025, e27567.

37 X. Li, M. Li, Z. Huang, G. Liang, Z. Chen, Q. Yang, Q. Huang and C. Zhi, Activating the I_0/I^+ redox couple in an aqueous I_2–Zn battery to achieve a high voltage plateau, *Energy Environ. Sci.*, 2021, **14**, 407–413.

38 F. Zhu, Z. Li, Z. Wang, Y. Fu and W. Guo, From Inorganic to Organic Iodine: Stabilization of I^+ Enabling High-Energy Lithium–Iodine Battery, *J. Am. Chem. Soc.*, 2024, **146**, 11193–11201.

39 T. Hu, Y. Zhao, Y. Yang, H. Lv, R. Zhong, F. Ding, F. Mo, H. Hu, C. Zhi and G. Liang, Development of Inverse-Opal-Structured Charge-Deficient Co_9S_8@nitrogen-Doped-Carbon to Catalytically Enable High Energy and High Power for the Two-Electron Transfer I^+/I^- Electrode, *Adv. Mater.*, 2024, **36**, 2312246.

40 C. Li, H. Li, X. Ren, L. Hu, J. Deng, J. Mo, X. Sun, G. Chen and X. Yu, Urea Chelation of I^+ for High-Voltage Aqueous Zinc–Iodine Batteries, *ACS Nano*, 2025, **19**, 2633–2640.

41 X. Kong, J. Zhang, X. Zhang, Z. Wang and D. Wang, Boosting Reversible Four-Electron Redox in Aqueous Zn-Iodine Batteries with Two Halogen Ionic Additives and a N, F Codoped Carbon Cathode, *ACS Appl. Energy Mater.*, 2025, **8**, 601–610.

42 Y. Xia, W. Li, H. Xu, F. Wei, S. Ke, H. Chen, H. Zhang, G. Guo, L. Ma, J. Wang and S. Liu, Tunable Mesoporous Porphyrin-Based Conjugated Polymer Capable of Boosting Four-Electron Zn-I_2 Batteries, *Adv. Funct. Mater.*, 2025, **35**, 2417283.